Newton

Article

Mapping the three-dimensional structure of faceted gold mesocrystals using coherent X-ray diffraction imaging

Graphical abstract

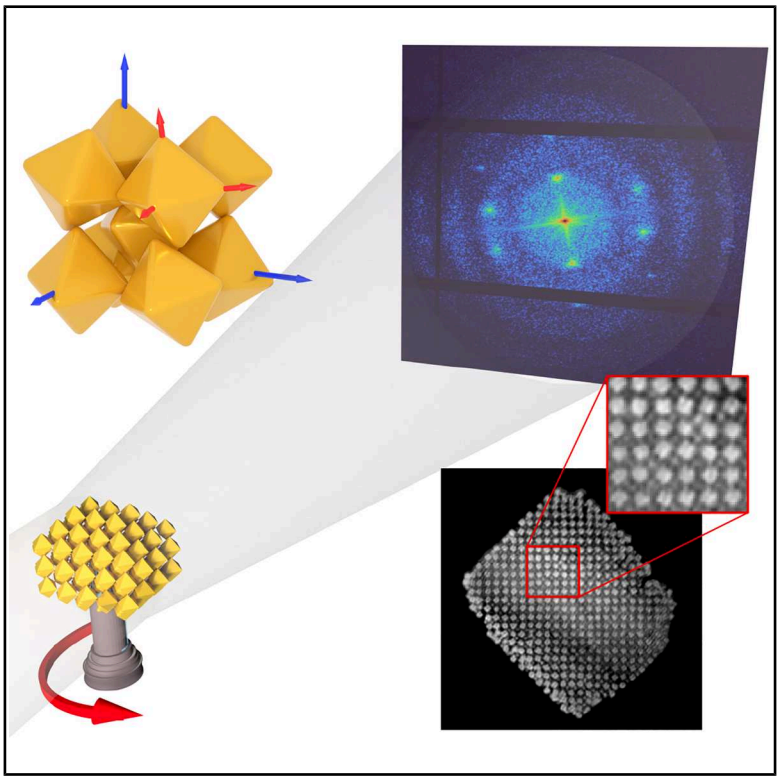

Highlights

- Mesocrystals assembled by Au nano-octahedra under different conditions are examined
- Coherent X-ray diffraction reveals the 3D structure of self-assembled mesocrystals
- Each faceted mesocrystal is found to have nearly defect-free lattice structures

Authors

Gerard N. Hinsley, Kuan Hoon Ngoi, Sebastian Sturm, ..., Knut Müller-Caspary, Elena V. Sturm, Ivan A. Vartanyants

Correspondence

sturm.elena@lmu.de (E.V.S.), ivan.vartaniants@desy.de (I.A.V.)

In brief

Understanding the structure-property relationship of self-assembled superstructures requires non-destructive 3D structural analysis, which can then facilitate the development of mesocrystals with collective and emergent properties. Hinsley et al. employ coherent X-ray diffractive imaging to resolve the positions and orientations of the constituent gold octahedral nanoparticles in multiple self-assembled mesocrystals as well as defects within the mesocrystal lattice structure.

Hinsley et al., 2026, Newton *2*, 100269
February 2, 2026
https://doi.org/10.1016/j.newton.2025.100269

CellPress

Newton

CellPress
OPEN ACCESS

Article

Mapping the three-dimensional structure of faceted gold mesocrystals using coherent X-ray diffraction imaging

Gerard N. Hinsley,[1] Kuan Hoon Ngoi,[1] Sebastian Sturm,[2] Rustam Rysov,[1,5] Felizitas Kirner,[3,6] Dmitry Lapkin,[1,7] Shweta Singh,[1] Dameli Assalauova,[1,8] Michael Sprung,[1] Thomas Wiek,[4] Thomas Gemming,[4] Axel Lubk,[4] Knut Müller-Caspary,[2] Elena V. Sturm,[3,*] and Ivan A. Vartanyants[1,9,*]

[1]Deutsches Elektronen-Synchrotron DESY, Notkestrasse 85, 22607 Hamburg, Germany
[2]Department of Chemistry and Center for NanoScience, Ludwig Maximilian University of Munich (LMU), Butenandtstrasse 11, 81377 Munich, Germany
[3]Department of Earth and Environmental Sciences and Center for NanoScience, Ludwig Maximilian University of Munich (LMU), Theresienstrasse 41C, 80333 Munich, Germany
[4]Leibniz Institute for Solid State and Materials Research, Helmholtzstrasse 20, 01069 Dresden, Germany
[5]Present address: European XFEL GmbH, Holzkoppel 4, 22869 Schenefeld, Germany
[6]Present address: Corden Pharma Switzerland LLC, Eichenweg 1, 4410 Liestal, Switzerland
[7]Present address: Institut für Angewandte Physik, Universität Tübingen, Auf der Morgenstelle 10, 72076 Tübingen, Germany
[8]Present address: Constructor University, Campus Ring 1, 28759 Bremen, Germany
[9]Lead contact
*Correspondence: sturm.elena@lmu.de (E.V.S.), ivan.vartaniants@desy.de (I.A.V.)
https://doi.org/10.1016/j.newton.2025.100269

ACCESSIBLE OVERVIEW Just as atoms are the building blocks for an atomic lattice in a crystal, nanoparticles may similarly act as building blocks to form a lattice in larger structures termed "colloidal crystals." Mesocrystals are a sub-type of colloidal crystal for which the nanoparticle building blocks are arranged with a high degree of translational and orientational order. Due to the highly ordered structure, mesocrystals can exhibit emergent properties such as localized surface plasmon (LSP), making them intriguing in several applications, including surface-enhanced Raman scattering, optical waveguides, and photocatalysis. The coupling strength of LSP and the resonance energy of the coupled modes are highly dependent on the structure, which itself is highly dependent on the initial growth conditions, including choice of nanoparticle building block. Therefore, to understand the structure-property relationship, it is imperative that non-destructive techniques are used to characterize in three dimensions the final self-assembled structures. In this article, we synthesized three mesocrystals under different growth conditions; then, using coherent X-ray diffraction, we characterized their 3D structural arrangement. We determined that the specific crystallization conditions produce mesocrystals with a nearly defect-free lattice structure, where higher strain is observed toward the surface and within the vicinity of cracks. These results demonstrate the potential of coherent X-ray diffraction analyses as a non-destructive tool to perform a detailed structural analysis of mesocrystalline structures, thereby unraveling the complex structure-property relationship of self-assembled nanoparticle assemblies. The increased coherent flux of diffraction-limited sources can aid future studies, allowing bigger mesocrystals to be measured with a higher spatial resolution as well as improving the ability to perform investigations into the structure-property relationships under external stimuli. Such studies will allow the resolving of complex structural features of self-assembled nanoparticle assemblies, enabling the precise tailoring of their properties.

SUMMARY

Elucidating the structure-property relationship of mesocrystals requires understanding the mutual arrangement of the nanoparticles within their assembly. This, therefore, requires characterization techniques capable of non-destructively distinguishing the shape, position, and orientation of the individual constituent nanoparticles in three dimensions. This detailed structural analysis is achieved here by using coherent X-ray

diffraction imaging (CXDI) complemented with angular X-ray cross-correlation analysis (AXCCA) and electron microscopy. Three mesocrystals are examined, each assembled from different-sized gold octahedral nanoparticles and functionalized with ω-thiol-terminated polystyrene (PS-SH) of different molecular weights. AXCCA provides information regarding the ensemble-averaged mesocrystal lattice structure, such as the symmetry, unit cell parameters, and the presence of orientational disorder. CXDI complementarily enables the precise identification of the shape and positions of individual nanoparticles as well as revealing any structural defects. Our results show that each mesocrystal has a nearly perfect lattice structure with minimal defects and exhibits an increased strain toward the surface.

INTRODUCTION

Just as atoms are the building blocks for an atomic lattice in a crystal, nanoparticles may similarly act as building blocks to form a lattice in a colloidal crystal.[1,2] The structure of such self-assembled lattices with a high degree of translational and orientational order (so-called mesocrystals[3,4]) is generally determined by the effective shape and composition of the nanoparticle building blocks and the balance between interparticle and particle-medium forces.[5–8] Unlike space-filling anisotropic nanoparticles, octahedral building blocks (when stabilized by different types of ligands) exhibit a wide variety of crystalline and liquid-crystalline structures with different orientational and translational orders.[9–12]

The Minkowski lattice is the densest packing array for regular hard octahedra with mutual alignment (packing density 18/19).[13] Nevertheless, the effective shape of real octahedral nanoparticles (from here on referred to as nano-octahedra) could significantly deviate from an ideal octahedron due to the truncation of edges and vertices and surface functionalization by organic capping molecules. Changes in ligand conformation, as well as specific ligand-ligand and ligand-solvent interactions, could additionally significantly influence the assembly process and final structure of the mesocrystal.[6,8,11,14–17] Therefore, it is challenging to predict the final structure of assembled materials under specific experimental conditions.

In our previous work, we systematically studied the dual effect of gold nano-octahedral size and chain length of ω-thiol-terminated polystyrene (PS-SH) capping molecules on the self-assembly and growth of colloidal crystals (e.g., mesocrystals) and their resulting crystal structure.[15] These mesocrystals were found to exhibit a rhombic-dodecahedral shape and, by performing angular X-ray cross-correlation analysis (AXCCA),[18–20] were determined to have a body-centered cubic (*bcc*) mesocrystal lattice.[15] In this mesocrystal lattice, gold nano-octahedra are predominantly arranged in a tip-to-tip configuration with some degree of angular disorder. This type of particle arrangement was recently categorized as a tip-on-tip configuration, in contrast to a tip-to-tip one, and is more favorable, as it enables more effective packing.[21] It has also been demonstrated that, in the case of tip-on-tip two-dimensional (2D) assemblies of gold nanobipyramids stabilized by pentaethylenehexamine-terminated polystyrene (PS-PEHA) ligands, surface-enhanced Raman scattering (SERS) signals show the highest enhancement factor.[21] Nevertheless, it is still unclear how this configuration is achieved and translated in three-dimensional (3D) assemblies (e.g., mesocrystals).

To solve this structural conundrum, in this study we apply coherent X-ray diffraction imaging (CXDI), which enables the reconstruction of the 3D structure of mesocrystals in real space with nanoscale spatial resolution. CXDI achieves this by using phase retrieval algorithms to recover the missing phase information when recording oversampled diffraction intensities, which then, through a Fourier relationship, provide information on the original object structure.[22–26] This allows for mapping structural distortions and different types of defects in the structure.[27–29] Previously, using this method, we were able to image and resolve the structure of a 3D self-assembled gold mesocrystal prismatic grain (cut out by using a focused ion beam [FIB] milling procedure on a faceted mesocrystal) composed of 60 nm nanocubes stabilized by cetylpyridinium chloride molecules.[30] It was, however, difficult to discriminate between defects caused by mesocrystal growth and defects caused by post-growth activities (including drying and FIB-cut preparation). To avoid these issues, in this study, we used as-grown rhombic-dodecahedral-shaped mesocrystals of a few micrometers in size built up from PS-SH-stabilized gold nano-octahedra. Furthermore, by varying the lengths of the PS-SH polymer chain, the distance between the nano-octahedra within the mesocrystals can be successfully tuned, which in turn impacts the accuracy with which we can distinguish the positions and shapes of individual nanoparticles.

Obtaining structural information in 3D is essential for understanding the structure-property relationship of nanoparticle assemblies, since interparticle distance, geometry, and short-range order of nanoparticles significantly influence the coupling strength of localized surface plasmons (LSPs) and resonance energy of the coupled modes. These unique optical properties of noble-metal nanoparticle assemblies (single and multi-component) are intriguing not only for fundamental research but also for several applications, for example, SERS, optical waveguides, photocatalysis, etc.[5,16,21,31–34] Therefore, a detailed structural characterization of assembled materials in real space is essential to identify the crucial parameters affecting their efficiency and performance and to optimize materials design.

RESULTS AND DISCUSSION

Sample preparation and data collection

We studied three different mesocrystal samples self-assembled from PS-SH-functionalized gold nano-octahedra using a gas-phase diffusion growth approach, as shown in Figure 1A. Further details about the sample preparation procedures can be found in

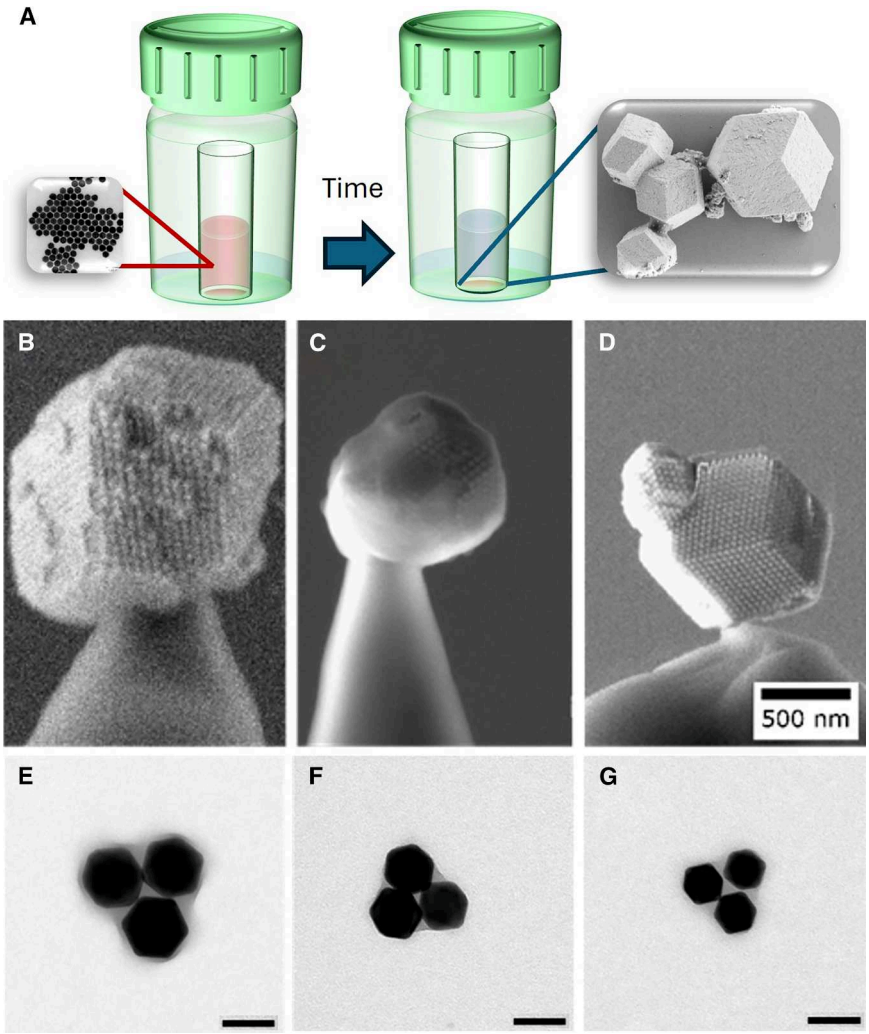

Figure 1. Synthesis methodology and analysis of the studied Au mesocrystals

(A) A sketched setup depicting the gas-phase diffusion approach used for the nano-octahedra self-assembly. The system consists of a closed vial containing the antisolvent (solution of ethanol and toluene in a 1:1 volume ratio) and a smaller vial containing the nano-octahedra dispersion in toluene (inset, left: exemplary transmission electron microscopy [TEM] image). Over time, the antisolvent leads to the destabilization of nano-octahedra, self-assembly to mesocrystals (inset, right: exemplary scanning electron microscopy [SEM] image), and discoloration of the dispersion. (B–D) SEM images that were obtained of the resulting mesocrystals, which had been picked up and glued to a tungsten tip. From left to right, these samples are labeled as S_1 (B), S_2 (C), and S_3 (D). The scale bar in (D) also applies to the SEM images of (B) and (C).

(E–G) Exemplary TEM images of the gold nano-octahedra used for mesocrystal self-assembly (scale bar corresponds to 50 nm), for S_1, S_2, and S_3, respectively.

Lapkin et al.[15] We designate the three mesocrystals that we examine here as S_1, S_2, and S_3, which respectively correspond to the sample types of O3, O4, and O5 as described in Lapkin et al.,[15] for which the combinations of edge length, l_{edge}, and polymer chain length used are presented in Table 1. The mesocrystals examined here are from the same batch, but differ from those examined in Lapkin et al.,[15] as they are smaller in size, allowing them to be suitable for analysis by CXDI. All faceted as-grown mesocrystals have diameters between 1 and 1.5 μm and were mounted onto tungsten needles and fixed with SEMGLU glue (Kleindiek Nanotechnik) by means of a Zeiss 1540XB CrossBeam FIB scanning electron microscope (Figures 1B–1D).

CXDI measurements were performed at the Coherence Applications beamline P10 at PETRA III (DESY, Hamburg, Germany), and Figure S1 depicts the experimental setup and geometrical parameters used. Each mesocrystal was positioned in the incident focused X-ray beam and rotated around the vertical axis, where an EIGER X 4M detector placed 5 m downstream measured the scattered intensity. One dataset for a mesocrystal consists of the collection of diffraction patterns over an angular range of 180° in increments of 0.5°; further details on the experiment are found in the methods. Five datasets were collected in total—two from S_1, two from S_2, and one from S_3. A summary of the experimental parameters specific for each dataset collected is displayed in Table S1.

These angular sets of diffraction patterns were then interpolated into 3D diffraction patterns for each sample, and sliced planes of the 3D reciprocal space intensities are shown in Figures 2A, 2C, and 2E, and Figures 2B, 2D, and 2F show the respective radial profiles of the scattered intensity as a function of the magnitude of the momentum transfer vector q. The interpolated 3D diffraction patterns were used for subsequent analysis using AXCCA and as the input into the CXDI iterative-phase retrieval process[35] to recover the original mesocrystal structure.

Ensemble lattice information from angular X-ray cross-correlation analysis

We employed AXCCA to analyze the angular correlations of the intensity distribution in 3D reciprocal space. The cross-correlation function (CCF), $C(q, \Delta)$, was generated from pairs of scattered intensities at momentum transfer values q with relative angles Δ (see methods for the definition of $C(q, \Delta)$). The calculations of $C(q, \Delta)$, covering a q range from 0.100 to 0.550 nm^{-1}, were stacked into a 2D correlation map, as shown in Figures 3A–3C. A *bcc* lattice model ($a = b = c$, $\alpha = \beta = \gamma = 90°$) was then used to refine the unit cell parameter a based on the correlation peaks in the maps. Detailed analysis procedures can be found in the supplemental information, as well as in Lapkin et al.[15,36] The correlated positions calculated from the model

Table 1. Structural parameters of the nano-octahedra and mesocrystal lattices

Parameter	Sample S_1	S_2	S_3
Molecular weight of PS-SH, M_w (kg mol^{-1})	43	22	22
Nano-octahedra edge length, l_{edge} (nm)	58.4 ± 1.8	46.3 ± 1.4	36.7 ± 1.1
Tip-to-tip distance, $d_{t\text{-}t}$ (nm)	79.5 ± 2.5	63.8 ± 2.3	51.5 ± 1.9
Facet-to-facet distance, $d_{f\text{-}f}$ (nm)	47.7 ± 1.5	37.8 ± 1.1	30.0 ± 0.9
Unit cell parameter, a (nm)	64.7 ± 1.2	55.4 ± 1.0	44.5 ± 0.4
First Bragg peak q value (nm^{-1})	0.137 ± 0.003	0.161 ± 0.003	0.200 ± 0.002
Unit cell angular distortion, $\Delta\varphi$ (°)	0.9 ± 0.3	1.4 ± 0.7	1.0 ± 0.4
Nearest-neighbor distance, d_{nn} (nm)	56.0 ± 1.0	48.0 ± 0.9	38.6 ± 0.3
Difference between d_{nn} and $d_{f\text{-}f}$ (nm)	8.3 ± 2.5	10.3 ± 2.0	8.6 ± 1.2

A summary of the structural parameters for the S_1, S_2, and S_3 samples obtained through TEM, AXCCA, and the Williamson-Hall method, as well as the molecular weight (M_w) values of PS-SH used to stabilize the Au nano-octahedra are provided. TEM measurements as described in Lapkin et al.[15] provide the average edge length l_{edge} of the nano-octahedra and were used to estimate the tip-to-tip distance ($d_{t\text{-}t} = \sqrt{2}l_{edge}$) and facet-to-facet distance ($d_{f\text{-}f} = \sqrt{2/3}l_{edge}$). The unit cell parameter a of the *bcc* mesocrystal lattice was refined from the AXCCA results, and the error values represent standard deviations (Δa) obtained from the Williamson-Hall method. The first Bragg peak corresponds to the reciprocal lattice vector length g_{110} of the refined unit cell. The unit cell angular distortions $\Delta\varphi$ and their respective error values were determined from the Williamson-Hall method. The nearest-neighbor distance ($d_{nn} = \sqrt{3}\,a/2$) was calculated from the unit cell parameter a.

lattice (marked by red circles in Figures 3A–3C) show good agreement with the peak positions in the map. Additionally, the Williamson-Hall method[37] (see details in the supplemental information) further complements the analysis by providing the standard deviation of the unit cell parameter Δa and the unit cell angular distortion $\Delta\varphi$. The structural parameters obtained in the AXCCA and Williamson-Hall methods are summarized in Table 1.

By considering the cubic symmetry of the *bcc* unit cell, the nearest-neighbor distance within the mesocrystal ($d_{nn} = \sqrt{3}a/2$) estimated the effective size of particles capped with a polymer shell to be 56.0 ± 1.0, 48.0 ± 0.9, and 38.6 ± 0.3 nm for samples S_1, S_2, and S_3, respectively. The difference between d_{nn} and the facet-to-facet distance ($d_{f-f} = \sqrt{2/3}l_{edge}$) is consistent with the presence of the polymer layer between facets of adjacent Au nano-octahedra (Table 1).

The octahedral form factor exhibits anisotropic X-ray scattering along the atomic lattice axes $<111>_{AL}$ and normal to each of the octahedron {111} facets, facilitating the examination of nano-octahedra orientation within a mesocrystal by comparing the experimental and simulated form factor scattering intensities in their respective sliced reciprocal planes (see details in the supplemental information). This analysis indicates the presence of orientational disorder among the nano-octahedra, which would otherwise result in a perfect tip-to-tip assembly (see Figures S11–S13)). As discussed in Lapkin et al.,[15] a perfect tip-to-tip assembly is a topologically unfavorable structure for this system. In this study, the standard deviation of nano-octahedra orientation ($\delta\varphi$) for all samples was estimated to be approximately 15°, aligning with previous findings in Lapkin et al.,[15] which can be described as a tip-on-tip configuration with some degree of angular disorder.[21] A visualization of a tip-on-tip configuration is displayed in Figure 3D, where the atomic lattice axes $[hkl]_{AL}$ of the nano-octahedra are shown to not directly align with the axes of the mesocrystal lattice $[hkl]_{ML}$.

Reconstructing 3D structures by coherent X-ray diffraction imaging

Three-dimensional CXDI reconstructions of the examined mesocrystals and representative slices of the reconstructed amplitude normal to the [100], [010], and [001] mesocrystal lattice crystallographic directions are shown in Figure 4. For samples S_1 and S_2, we were able to reconstruct not only the mesocrystal but also the supporting tungsten tip to which the mesocrystal was attached, letting us relate the positioning of the tip to any induced structural defects. Details of the reconstruction parameters can be found in the methods. For samples S_1 and S_2, the reconstructions of the dataset with the highest spatial resolution are shown in Figure 4. We determined the resolution of the reconstruction by the phase retrieval transfer function (PRTF),[36] with results provided in the methods and supplemental information. Reconstructions of the extra datasets are also supplied in the supplemental information.

An isosurface of the reconstructed amplitude (Figures 4A, 4C, and 4E) reveals a slightly deformed rhombic-dodecahedral shape for all *bcc* mesocrystals and matches the shape observed in the scanning electron microscopy (SEM) images shown in Figures 1B–1D. In the case of the S_3 sample, an extra particle growth is also visible on the surface. Previous studies have also shown that self-assemblies of nanoparticles stabilized by organic ligands with a *bcc* superstructure tend to grow in the form of a rhombic dodecahedron.[38,39] The rhombic dodecahedron is a thermodynamic equilibrium shape of atomic crystals (e.g., metals) with *bcc* structure and, therefore, has a minimum surface energy in comparison to other crystallographic forms.[40] Nevertheless, in real crystallization conditions, the shape of *bcc* metallic crystals very rarely resembles a rhombic dodecahedron. This is due to the deviation from equilibrium of crystal growth conditions and specific interactions of medium species with the facets of growing crystals, which could significantly modify their surface energy. Therefore, the fact that the presented *bcc* mesocrystals show a rhombic-dodecahedral shape indicates that the selected crystallization conditions allow for obtaining

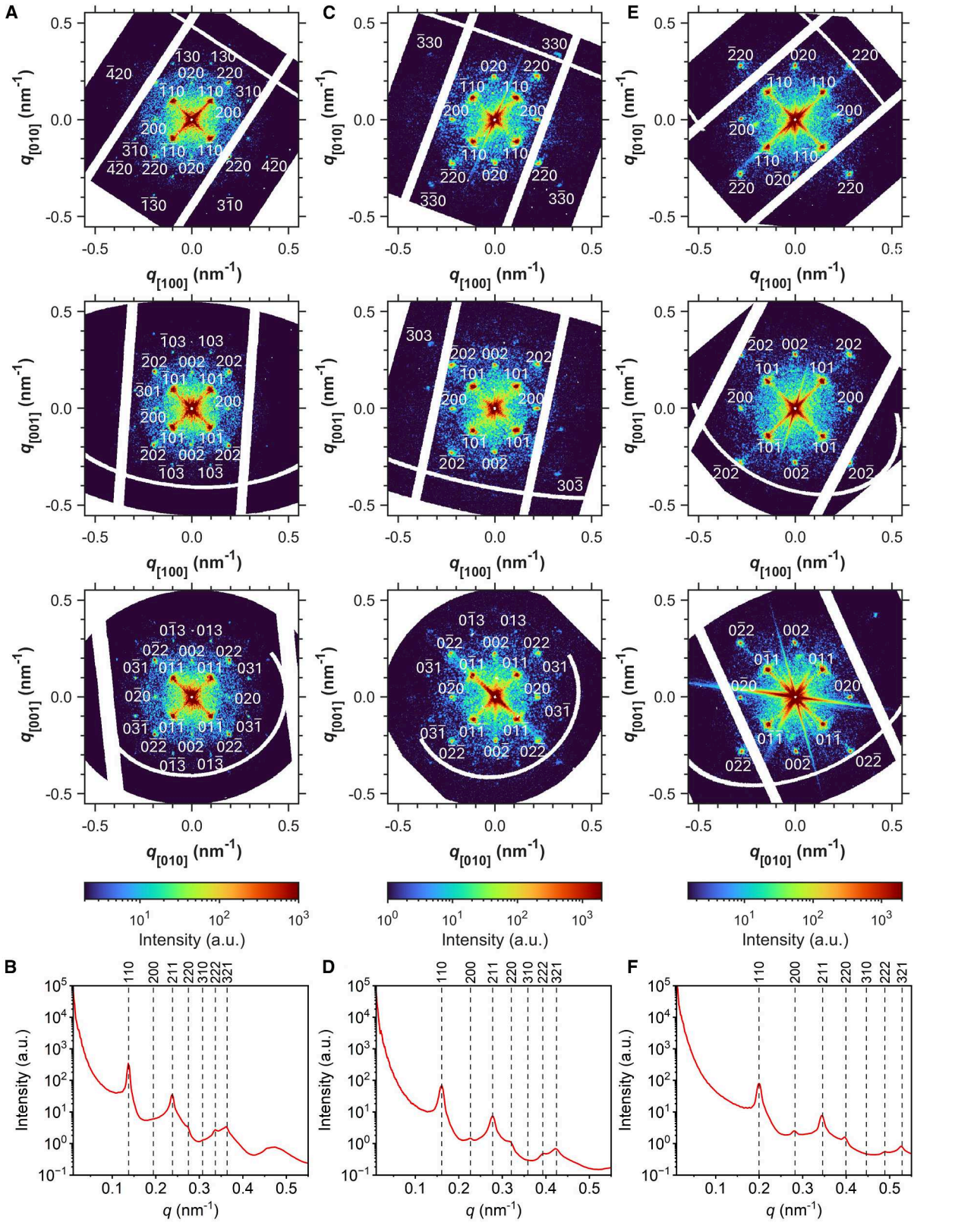

(legend on next page)

mesocrystals with a morphology close to the thermodynamic equilibrium shape of crystals with ideal *bcc* structure.[41,42]

The 2D cuts, shown in Figures 4B, 4D, and 4F, allow for visualization of the internal structural arrangement of the nano-octahedra. Here, the slices of the mesocrystals were selected such that they are incident with the waist of the nano-octahedra to highlight their size, and so different point defects within the mesocrystal lattice can be readily identified. The obtained CXDI reconstruction quality is sufficient not only to identify the locations of nano-octahedra as well as defects within the mesocrystal lattice, but due to the larger particle size for S_1, we are also able to distinguish the individual shape and orientation of some nano-octahedra. By examining the magnified image in Figure 4B, we observe some orientational disorder between adjacent octahedra, and as such we can visually confirm the tip-on-tip structural configuration suggested in the previous section (Figure 3D). The spatial resolution is insufficient in the current study to allow the same visual observation to be made for S_2 and S_3. Similar cuts for the extra particle growth in S_3 are presented in Figure S23. This particle has a high degree of structural disorder and as such, also due to insufficient resolution, it is difficult to identify mesocrystal lattice structure.

Structural analysis of mesocrystals

The position of each nano-octahedra within the mesocrystal lattices of S_1, S_2, and S_3 (shown in three directions in Figures S14–S22, A and E) was identified using a "blob detection" algorithm (see methods) and further refined manually, where mesocrystals S_1 and S_3 were each found to consist of around 10,000 nano-octahedra, while sample S_2 consists of only ca. 3,600 nano-octahedra. The extracted positions of all of the nano-octahedra for the entirety of the mesocrystal structures are displayed as 3D scatterplots in Figures S14–S22, B, as well as for a central slice (100 nm thickness) through each mesocrystal in Figures 5A, 5D, and 5G and S14–S22, F. Assuming that AXCCA is giving one the ensemble average structure, we can calculate the full displacement field (see methods). The corresponding displacement field is shown in Figures 5B, 5E, and 5H (central slice 100 nm, five times increased) and Figures S14–S22, C and G (three times increased). These results demonstrate that, in general, there are stronger distortions of the mesocrystal lattice toward the mesocrystal surface and in close vicinity of cracks, which are believed to have been introduced by the tip of the tungsten needle during sample pickup.

Except for the cracks near the tungsten tip and defects near the surface, the mesocrystals have a nearly perfect lattice structure with only very small deviations, which is, apart from very few point defects, virtually defect free. This can also be confirmed by the dilatation (i.e., the sum of diagonal elements [trace] of the strain tensor), which was derived from the Cauchy strain tensor[43] and calculated in 3D over the entirety of the mesocrystals. This is visualized in Figures S14–S22, D, for the whole of the structures, as well as for a single central slice in Figures 5C, 5F, and 5I and S14–S22, H. While the magnitude of dilatation inside the mesocrystals is relatively low, they exhibit growing (predominantly compressive) strain toward the mesocrystal surface. 3D visualization of the reconstructions (both phase and amplitude), as well as the structural analysis (nanoparticle positions, displacements, and dilatation), are shown in Videos S1–S11 for sample S_1, Videos S12–S22 for sample S_2, and Videos S23–S33 for sample S_3.

Furthermore, we examined the distribution of the nano-octahedral positions for each mesocrystal by calculating the pair-distribution function (PDF), for which the results are shown in Figure 6. At small distances r, the PDF values obtained using the experimental data match reasonably well with that using the ideal model mesocrystal lattice using the unit cell parameters obtained by AXCCA. At larger r, the PDF tends to smooth out and no longer matches the ideal AXCCA lattice, which is expected due to the structural distortions present in the crystal.

The insets in each of Figures 6A, B, and C show a magnified image of the first few PDF peaks. At the positions where we expect to see the first two peaks corresponding to the nearest-neighbor distance, d_{nn}, as well as the unit cell parameter, a, we instead see a single broad peak with a shoulder on the right-hand side. This is more pronounced for the S_2 sample shown in Figure 6B. The shape of this peak was fitted using two Gaussian functions to estimate the average distances to neighboring particles, where the standard deviation of the fits also provides an upper-bound estimate for the accuracy with which we can identify nano-octahedral positions, as the spread is also affected by mesocrystal lattice distortions. Plots showing the fits for these two peaks are included in the insets, where the fit corresponding to the nearest-neighbor distance peak, d_{nn}, is shown in magenta, while the fit for the unit cell parameter peak, a, is shown in blue. The obtained peak positions and standard deviations for each sample are $d_{nn}^{\mathrm{PDF}} = 57.0 \pm 4.6$ nm and $a^{\mathrm{PDF}} = 65.8 \pm 5.6$ nm (S_1, Figure 6A), $d_{nn}^{\mathrm{PDF}} = 48.8 \pm 2.8$ nm and $a^{\mathrm{PDF}} = 56.4 \pm 3.6$ nm (S_2, Figure 6B), and finally $d_{nn}^{\mathrm{PDF}} = 39.5 \pm 4.1$ nm and $a^{\mathrm{PDF}} = 45.6 \pm 4.2$ nm (S_3, Figure 6C). These values match quite closely to values obtained by AXCCA displayed in Table 1, indicating accurate fitting of the data. Extra magnified plots of the PDF are presented in Figure S24 in the supplemental information, which include the overall fit to the reconstructed data as well as the expected peak positions in the ideal AXCCA cell.

Conclusion

This work has demonstrated how the use of coherent X-ray diffraction techniques, AXCCA and CXDI, combined with SEM

Figure 2. Examination of the 3D reciprocal space

(A, C, and E) Sliced reciprocal planes of the 3D intensities through the origin for samples S_1 (A), S_2 (C), and S_3 (E) showing the planes (from top to bottom) normal to the mesocrystal lattice axis $[001]_{\mathrm{ML}}$, normal to the mesocrystal lattice axis $[010]_{\mathrm{ML}}$, and normal to the mesocrystal lattice axis $[100]_{\mathrm{ML}}$. The index of each Bragg peak is indicated. The white regions in the images are unmeasured as they correspond to gaps in the detector or are beyond the detector pixel array.

(B, D, and F) Radial intensity profiles of the scattered intensity are shown on a logarithmic scale as a function of the magnitude of the momentum transfer vector q for samples S_1 (B), S_2 (D), and S_3 (F). The dashed lines show the diffraction positions of the Bragg peaks. The intensity of the family of Bragg peaks in the order of {200} in S_1 and {310} in all samples is diminished due to their proximity to the minima of the form factor.

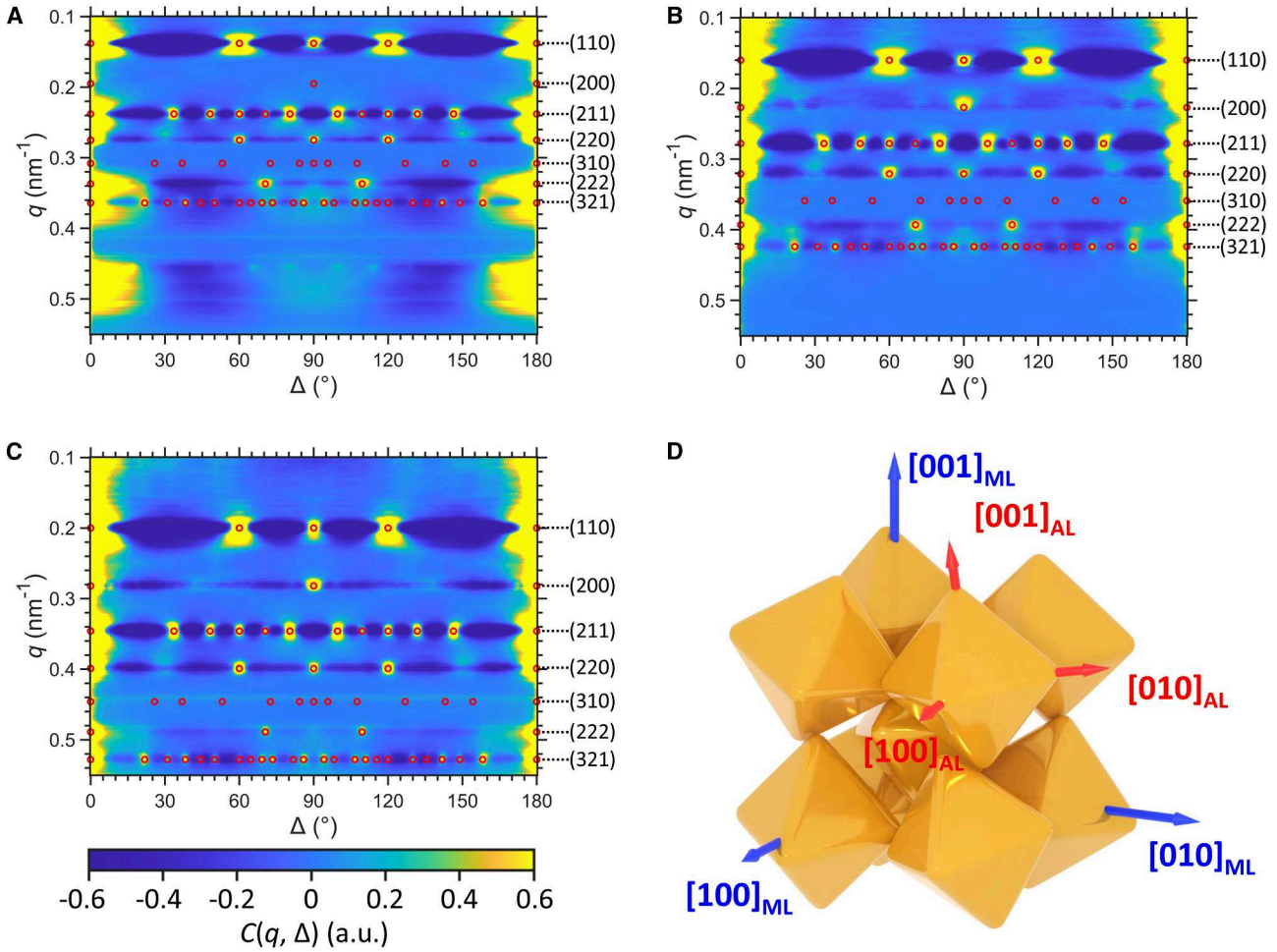

Figure 3. Angular X-ray cross-correlation analysis maps of the mesocrystal lattice structure

(A–C) Two-dimensional correlation maps were generated for samples S_1 (A), S_2 (B), and S_3 (C) over a q range of 0.100–0.550 nm^{-1}, with a step size of 0.001 nm^{-1}. The horizontal axis shows the relative angle Δ, the left vertical axis corresponds to the magnitude of the momentum transfer vector q, and the right vertical axis indicates the diffraction peak positions. The color bar represents the correlation values of $C(q, \Delta)$ displayed in the maps. The theoretical positions corresponding to the refined *bcc* lattice were computed and are indicated in red circles.

(D) The nano-octahedra assembled within a *bcc* unit cell, displaying the presence of orientational disorder corresponding to a tip-on-tip configuration.

and improved sample preparation and handling methods can elucidate the detailed structural properties of mesocrystalline structures and their constituent nanoparticles. This complementary analysis was performed on three mesocrystals, each synthesized with gold nano-octahedra of different edge lengths and functionalized by PS-SH with different molecular weights.

By analyzing the ensemble-averaged mesocrystal lattice structure by AXCCA, it was determined that, for each mesocrystal, the nano-octahedra assemble into a *bcc* lattice in a tip-on-tip structural arrangement, consistent with previous studies on these mesocrystals.

CXDI reconstructions were then performed on the same datasets, providing real-space 3D images of the mesocrystals, allowing for the position of each nano-octahedron to be resolved while also providing insights into defects within the structure. In the case of the S_1 sample, the shapes of the nano-octahedra were also resolved, which confirmed the tip-on-tip structural arrangement. It was found that, under these growth conditions, the mesocrystals grow in the form of a rhombic dodecahedron, where, excluding some point defects and cracks near the attachment of the tungsten tip, each mesocrystal self-assembled into a structure with a nearly defect-free mesocrystal lattice structure. From 3D displacement fields and strain tensors, calculated by knowing the positions of individual nano-octahedra, each mesocrystal is shown to exhibit stronger lattice distortions closer to the surface of the mesocrystal and in the vicinity of cracks.

These results imply that the crystallization conditions used allow one to obtain faceted mesocrystals with a nearly defect-free lattice structure. It was shown recently that a high degree of mesocrystal lattice order and a tip-on-tip configuration of nanocrystals are highly beneficial for potential applications of plasmonic active materials.[21,33] Further studies of potential applications of mesocrystals could significantly benefit from exploring the

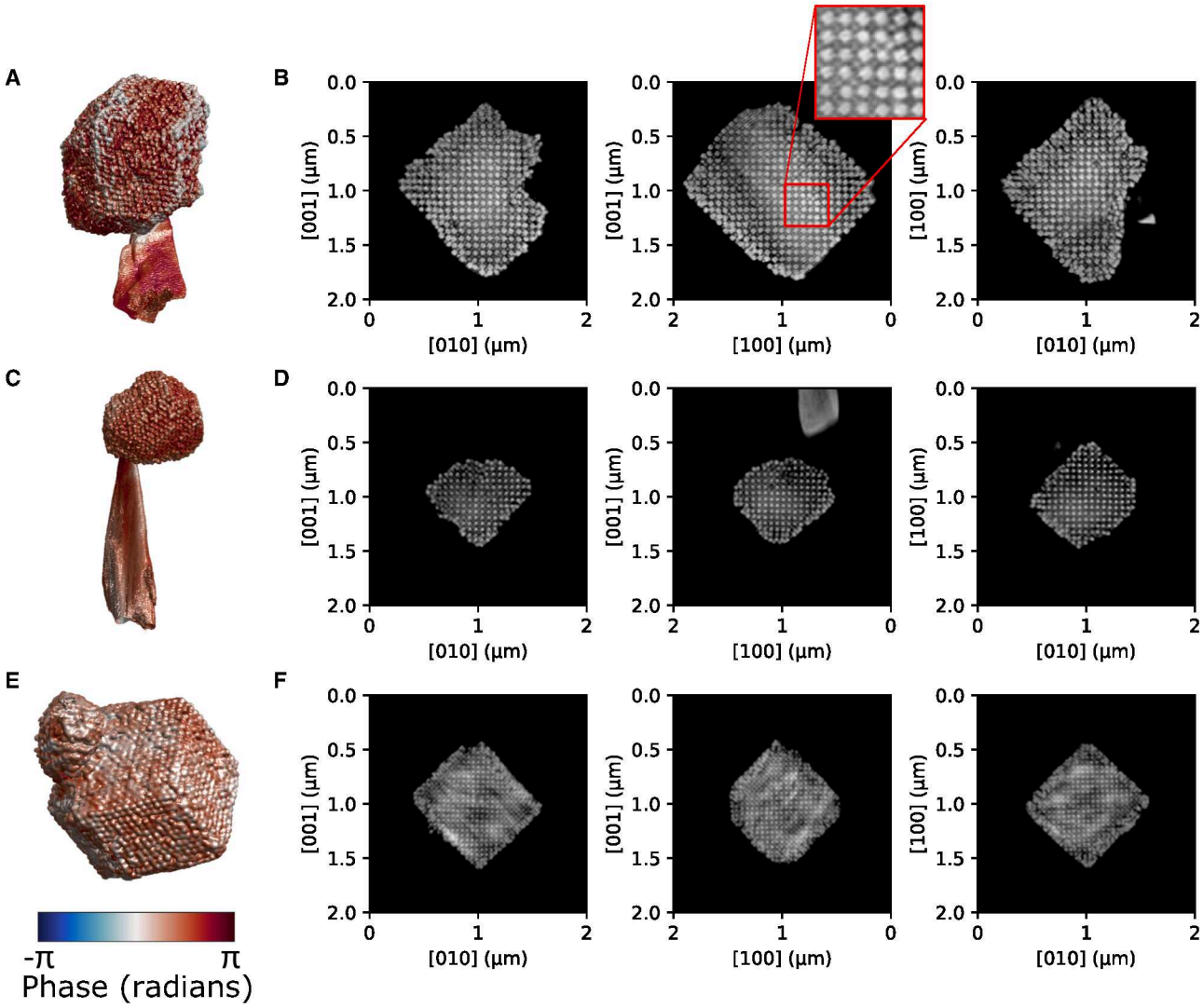

Figure 4. Real-space mesocrystal structures obtained by coherent X-ray diffraction imaging

(A, C, and E) Three-dimensional isosurfaces calculated at 10% of the maximum of the reconstructed amplitude for S_1, S_2, and S_3, respectively, where the color represents the value of the reconstructed phase. The view was chosen to match closely the SEM images in Figures 1B–1D.

(B, D, and F) Two-dimensional cuts obtained near the center of mass of the reconstructed amplitude normal to the (from left to right) [100], [010], and [001] crystallographic directions of the mesocrystals. The red box in (B) shows a magnified image of the nano-octahedra for S_1 allowing visualization of the slight orientational disorder in their arrangement, which is indicative of a tip-on-tip configuration.

structure-property relationship under external stimuli (including temperature, pressure, magnetic and electric fields, etc.).[44,45]

Altogether, these results demonstrate the potential of coherent X-ray diffraction analysis as a non-destructive tool to provide the required detailed structural analysis of mesocrystalline structures. This analysis improves our understanding of how each controllable parameter in the self-assembly process affects the final resulting structure, which facilitates the development of well-tailored defect-free 3D mesocrystals with collective and emergent properties. This is, therefore, a crucial development to unravel the complex structure-property relationship of self-assembled nanoparticle assemblies.

This study also highlights the significance of diffraction-limited light sources[46,47] in providing an intense X-ray beam with a higher coherent fraction, which will allow one to measure bigger mesocrystals with higher spatial resolution. That will allow resolving of complex structural features of self-assembled nanoparticle assemblies and enable the precise tailoring of their properties.

METHODS

Synthesis of nanoparticles and their self-assembly to mesocrystals

The synthesis of CPC (hexadecylpyridinium chloride)-stabilized octahedral gold nanoparticles was performed using a previously optimized three-step seed-mediated synthesis technique.[48] In this process, the targeted shape and size of the nanoparticles was achieved by adjusting the concentration of the gold seeds,

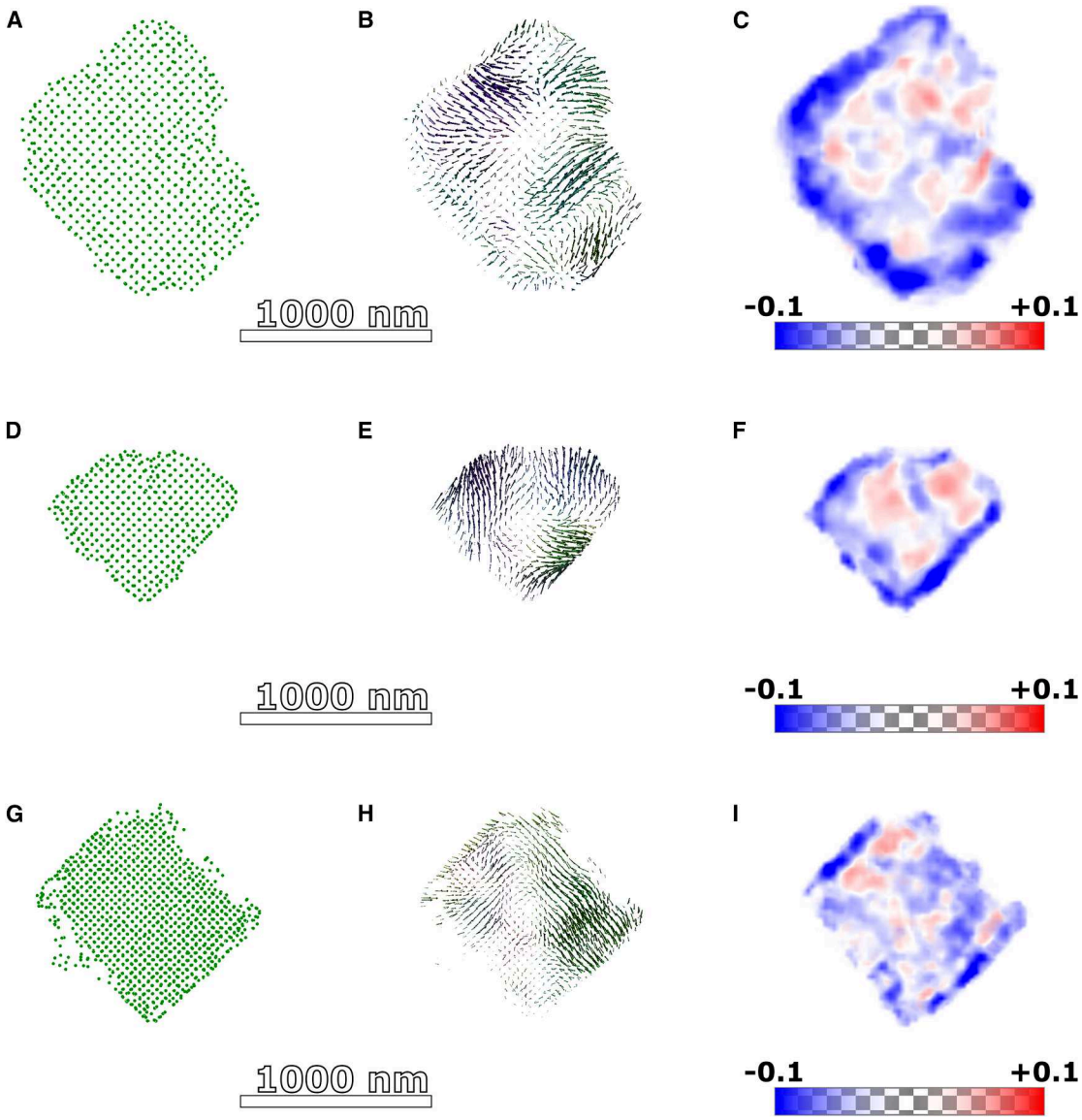

Figure 5. Structural insights of the mesocrystal structures

Structural analysis of samples S_1, S_2, and S_3, shown in the [100] direction of the *bcc* mesocrystal lattice for only the central (100) slice (thickness 100 nm) of the mesocrystal. (A, D, and G) Scatterplot of individual nano-octahedra positions. (B, E, and H) 3D vector plot of the displacement field (vector scale five times increased). (C, F, and I) Volume rendering of the mesocrystal lattice dilatation. Scale bar of 1,000 nm is indicated and applies to all images.

KBr, and ascorbic acid. Subsequent replacement of CPC ligands with polystyrene macromolecules was carried out by transferring the nanoparticles from an aqueous solution to toluene. Afterward, the self-assembly of nanoparticles into mesocrystals was conducted using a gas-phase diffusion technique, as shown schematically in Figure 1A. The toluene nanoparticle dispersion was gradually destabilized by the slow diffusion of the antisolvent (a 1:1 volume mixture of ethanol and toluene). The growth of the mesocrystals took ca. 2–3 weeks.[15]

Synchrotron X-ray experiment

Monochromatic X-rays of 12.65 keV were focused using compound refractive lenses (CRLs) down to 2.6 × 2.8 μm^2 (H × V) at the sample position, covering the mesocrystal. Each sample was fixed on an air-bearing stage, allowing rotation of the sample around the vertical axis. To limit radiation damage of the surfactant stabilizing the nano-octahedra, which could induce particle coalescence and destroy the mesocrystal lattice ordering, the samples were cooled using a liquid nitrogen cryostream to about 100 K. An EIGER X 4M detector was placed about 5 m downstream of the samples and far-field diffraction patterns were collected over an angular range of 180° in increments of 0.5°, with an exposure time between 3 and 5 s per projection. A beamstop was used to block the central beam and consisted of a tungsten cylinder glued on an Si wafer with dimensions 3 mm × 3 mm × 100 μm

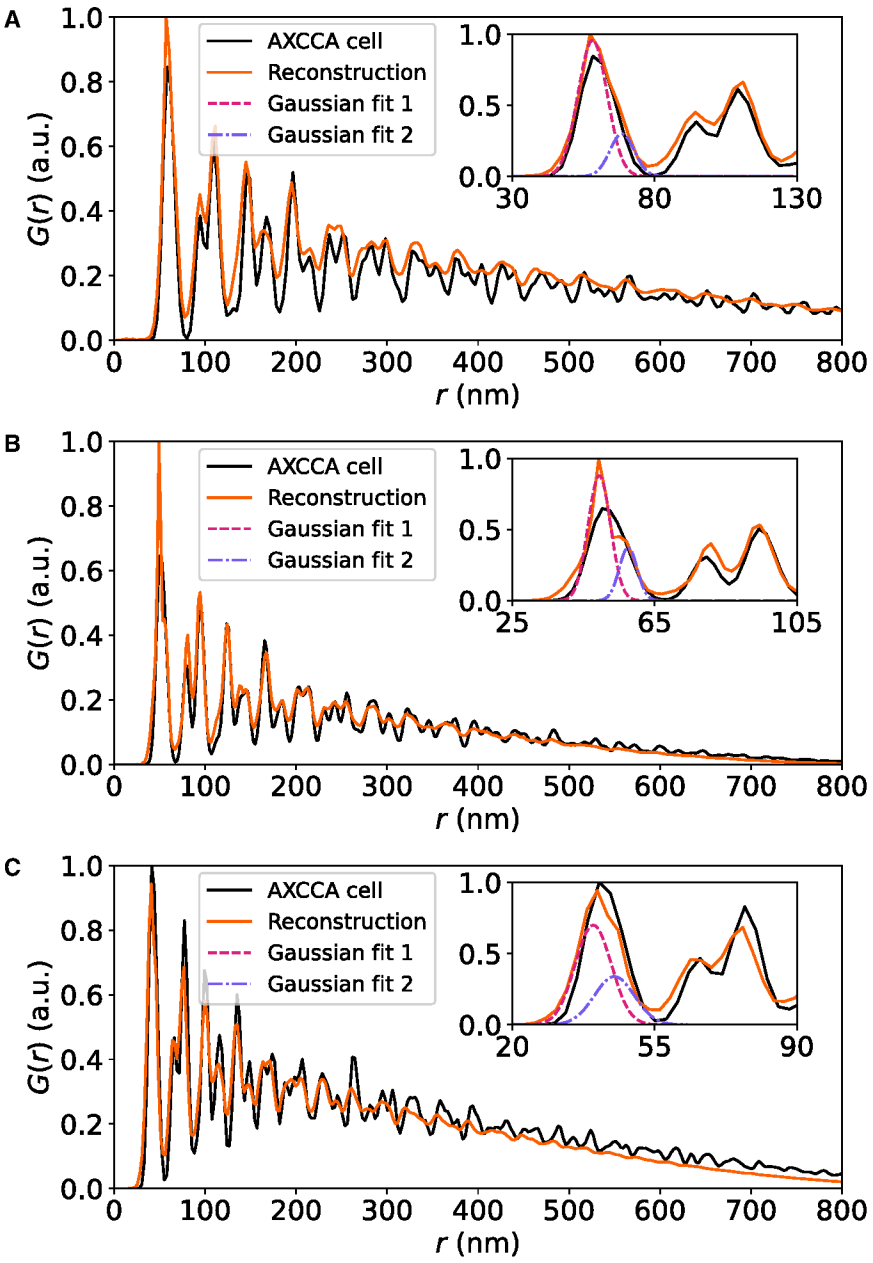

Figure 6. Particle-to-particle distance examination through the pair-distribution function

Pair-distribution functions (PDFs) obtained for samples S_1 (A), S_2 (B), and S_3 (C) showing the simulated average mesocrystal lattice (with broadening) as determined by AXCCA (black lines) and that obtained from the reconstructed data (red-orange lines). The insets show an enlarged region around the first few peaks, where the first two expected peaks correspond to the nearest-neighbor distance, d_{nn}, and the unit cell parameter, a. For S_1 and S_3, the peaks are combined due to the limited resolution, where a small shoulder can be observed, while for S_2, both peaks are better resolved but still overlapping.

(V × H × W), which was itself glued on another Si wafer with dimensions 5 mm × 5 mm × 100 μm (V × H × W). During data collection, some samples (see supplemental information) were translated in both horizontal and vertical directions to re-center its position within the beam. This was performed after every 5° increment.

Data processing

Several preprocessing steps were applied to the as-collected data before they were analyzed. First, the position of the beam center at the detector was identified, and data were cropped to a size of 1,152 × 1,152 pixels around this position. To account for pixels affected by the Si wafer beamstop, the X-ray absorption at 12.65 keV was calculated and used to scale the intensities. Some projections exhibited lower than expected intensity, which is attributed to poor alignment of the sample within the beam. Projections identified with this issue were scaled such that the intensity for a given projection matched that of adjacent projections. The data were then binned by a factor of 2, and the stack of 2D projections was interpolated at each angular position to an orthonormal frame to produce the full 3D diffraction intensity. The result of this process for each sample is shown in Figure 2, showing sliced planes of the 3D intensity.

A pixel mask was simultaneously created to remove dead pixels, gaps in the detector modules, and the effect of the tungsten beamstop, for which a radius of 6 pixels at the beam center was excluded. In Figure 2, large streaks in the intensity are observed due to diffraction from the tungsten tip. For the S_3 sample, these streaks were masked before reconstruction, while they were left untouched for samples S_1 and S_2. The masked diffraction intensity for sample S_3 is shown in the supplemental information.

Angular X-ray cross-correlation analysis

AXCCA was employed to characterize the ensemble average packing arrangement of gold nano-octahedra within the mesocrystals.[15] In this analysis, the CCFs between any pair of scattered intensities in 3D reciprocal space were calculated as

$$C(q,\Delta) = C(\mathbf{q}_1,\mathbf{q}_2,\Delta) = \left\langle \tilde{I}(\mathbf{q}_1)\tilde{I}(\mathbf{q}_2)\,\delta\left(\frac{\mathbf{q}_1\mathbf{q}_2}{|\mathbf{q}_1||\mathbf{q}_2|} - cos\Delta\right)\right\rangle, \quad \text{(Equation 1)}$$

where $\tilde{I}(\mathbf{q}_1)$ and $\tilde{I}(\mathbf{q}_2)$ are the scaled intensities corresponding to the momentum transfer vectors $\mathbf{q}_1$ and $\mathbf{q}_2$, with $|\mathbf{q}_1| = |\mathbf{q}_2| = q$, $\langle ... \rangle$, and Δ is the relative angle between the vectors. The averaging $\langle ... \rangle$ was performed over all scattered intensities at magnitude q, and $\delta(x)$ denotes the Kronecker delta function. The scattered intensities were scaled to their mean intensity at magnitude q as follows:

$$\tilde{I}(\mathbf{q}) = \frac{I(\mathbf{q}) - \langle I(\mathbf{q}) \rangle}{\langle I(\mathbf{q}) \rangle} . \qquad \text{(Equation 2)}$$

The CCFs were calculated in the q range from 0.100 to 0.550 nm^{-1} with a step size of 0.001 nm^{-1} and stacked along the vertical axis of q to obtain a 2D correlation map with relative angles Δ as its horizontal axis (shown in Figures 3A–3C).

Phase retrieval

The PyNX package[49] was used to perform the iterative algorithm process, which consisted of a sequence of 1,000 hybrid input-output (HIO)[35,50] + 2,000 relaxed averaged alternating reflections (RAARs)[51] + 2,000 error reduction (ER) iterations.[35,52] Modulus and support constraints were applied every iteration, with an initial support supplied to the reconstruction. Pixels within the mask were allowed to fluctuate and were not constrained. Partial coherence correction through the Lucy-Richardson deconvolution,[53] as implemented in PyNX, was used. The shrinkwrap algorithm[54] was applied every 30 iterations, where the threshold value ranged between 0.08 and 0.12 of the maximum amplitude value. For each sample, an initial reconstruction was performed, where the starting support was the autocorrelation function of the 3D diffraction intensity. The support from this reconstruction was then used as the starting guess for 20 further reconstructions in order to reduce the prevalence of twin image solutions. From this set of reconstructions, the best five, as judged by the lowest free log likelihood, were then used to perform a modal decomposition where the mode with the highest weighting represents the final object. After modal decomposition, the weighting of the first mode was taken as the final result and was 88%, 89%, and 89% for samples S_1, S_2, and S_3, respectively.[55] The voxel size in the reconstructions was 5.7 × 5.7 × 5.7 nm. The quality of each reconstructed result was determined by PRTF,[56] where a criterion value of 1/e was used to estimate the resolution (see the supplemental information). The resolution of the reconstructions in Figure 4 determined by the PRTF were 17 nm for S_1, 28 nm for S_2, and 26 nm for S_3, all of which were below the l_{edge} of the nano-octahedra. Results for all reconstructions are shown in the supplemental information.

Nanoparticle detection and structural analysis of mesocrystal lattices

The positions of the individual nano-octahedra within each mesocrystal were first detected using a blob detection algorithm on varying intensity threshold levels after varying low-pass filters while considering reasonable size constraints. The so-obtained sets of estimated 3D positions of nano-octahedra afterward were refined manually by comparing slices through the mesocrystal in all three dimensions. These sets of nano-octahedral positions were then matched against an ideal reference of the averaged mesocrystal lattice determined by AXCCA. The obtained displacement field for nano-octahedral positions ultimately yielded the full strain tensor of the mesocrystal lattice. The dilatation was calculated by taking the trace of the strain tensor.

Further details regarding the methods can be found in the supplemental information.

RESOURCE AVAILABILITY

Lead contact

Requests for further information and resources should be directed to and will be fulfilled by the lead contact, Ivan A. Vartanyants (ivan.vartaniants@desy.de). Correspondence may also be directed to Elena V. Sturm (sturm.elena@lmu.de).

Materials availability

This study did not generate new unique reagents.

Data and code availability

- All data reported in this paper may be shared by the lead contact upon reasonable request.
- This paper does not report original code.
- Any additional information required to reanalyze the data reported in this paper is available from the lead contact upon request.

ACKNOWLEDGMENTS

We appreciate the Helmholtz Association HGF and DESY (Hamburg, Germany) for providing the experimental facilities. We would like to thank the beamline employees for their support in using the Coherence Application P10 beamline during the process of this research, which was conducted in part at the PETRA III synchrotron facility. This research was supported in part through the Maxwell computational resources operated at Deutsches Elektronen-Synchrotron DESY, Hamburg, Germany. S. Sturm and K.M.-C. acknowledge support from the Bavarian Hightech Agenda (Germany) within the EQAP project.

AUTHOR CONTRIBUTIONS

Conceptualization, I.A.V. and E.V.S.; formal analysis, G.N.H., K.H.N., and S. Sturm; investigation, F.K., D.L., S. Singh, D.A., T.W., T.G., A.L., K.M.-C., E.V. S., and I.A.V.; resources, R.R. and M.S.; supervision, E.V.S. and I.A.V.; writing – original draft, G.N.H., K.H.N., S. Sturm, E.V.S., and I.A.V.; writing – review & editing, all authors.

DECLARATION OF INTERESTS

The authors declare no competing interests.

SUPPLEMENTAL INFORMATION

Supplemental information can be found online at https://doi.org/10.1016/j.newton.2025.100269.

Received: March 10, 2025
Revised: July 11, 2025
Accepted: September 26, 2025
Published: October 21, 2025

REFERENCES

1. Talapin, D.V. (2012). Nanocrystal solids: A modular approach to materials design. MRS Bull. *37*, 63–71. https://doi.org/10.1557/mrs.2011.337.

2. Lapkin, D., Kirsch, C., Hiller, J., Andrienko, D., Assalauova, D., Braun, K., Carnis, J., Kim, Y.Y., Mandal, M., Maier, A., et al. (2022). Spatially resolved fluorescence of caesium lead halide perovskite supercrystals reveals quasi-atomic behavior of nanocrystals. Nat. Commun. *13*, 892. https://doi.org/10.1038/s41467-022-28486-3.

3. Sturm Née Rosseeva, E.V., and Cölfen, H. (2016). Mesocrystals: structural and morphogenetic aspects. Chem. Soc. Rev. *45*, 5821–5833. https://doi.org/10.1039/C6CS00208K.

4. Sturm née Rosseeva, E., and Cölfen, H. (2017). Mesocrystals: Past, Presence, Future. Crystals *7*, 207.

5. Boles, M.A., Ling, D., Hyeon, T., and Talapin, D.V. (2016). The surface science of nanocrystals. Nat. Mater. *15*, 141–153. https://doi.org/10.1038/nmat4526.

6. Schlotheuber né Brunner, J., Maier, B., Thomä, S.L.J., Kirner, F., Baburin, I.A., Lapkin, D., Rosenberg, R., Sturm, S., Assalauova, D., Carnis, J., et al. (2021). Morphogenesis of Magnetite Mesocrystals: Interplay between Nanoparticle Morphology and Solvation Shell. Chem. Mater. *33*, 9119–9130. https://doi.org/10.1021/acs.chemmater.1c01941.

7. Batista, C.A.S., Larson, R.G., and Kotov, N.A. (2015). Nonadditivity of nanoparticle interactions. Science *350*, 1242477. https://doi.org/10.1126/science.1242477.

8. Simon, P., Rosseeva, E., Baburin, I.A., Liebscher, L., Hickey, S.G., Cardoso-Gil, R., Eychmüller, A., Kniep, R., and Carrillo-Cabrera, W. (2012). PbS–Organic Mesocrystals: The Relationship between Nanocrystal Orientation and Superlattice Array. Angew. Chem. Int. Ed. Engl. *51*, 10776–10781. https://doi.org/10.1002/anie.201204583.

9. Fan, Z., and Grünwald, M. (2019). Orientational Order in Self-Assembled Nanocrystal Superlattices. J. Am. Chem. Soc. *141*, 1980–1988. https://doi.org/10.1021/jacs.8b10752.

10. Lee, Y.H., Shi, W., Lee, H.K., Jiang, R., Phang, I.Y., Cui, Y., Isa, L., Yang, Y., Wang, J., Li, S., and Ling, X.Y. (2015). Nanoscale surface chemistry directs the tunable assembly of silver octahedra into three two-dimensional plasmonic superlattices. Nat. Commun. *6*, 6990. https://doi.org/10.1038/ncomms7990.

11. Ni, R., Gantapara, A.P., de Graaf, J., van Roij, R., and Dijkstra, M. (2012). Phase diagram of colloidal hard superballs: from cubes via spheres to octahedra. Soft Matter *8*, 8826–8834. https://doi.org/10.1039/C2SM25813G.

12. Xie, S., Zhou, X., Han, X., Kuang, Q., Jin, M., Jiang, Y., Xie, Z., and Zheng, L. (2009). Supercrystals from Crystallization of Octahedral MnO Nanocrystals. J. Phys. Chem. C *113*, 19107–19111. https://doi.org/10.1021/jp907651d.

13. Minkowski, H. (1904). Dichteste gitterförmige Lagerung kongruenter Körper. Nachr. Ges. Wiss. Göttingen, Math.-Phys. Kl *1904*, 311–355.

14. Chumakova, A., Kirner, F., Chumakov, A., Roth, S.V., Bosak, A., and Sturm, E.V. (2023). Exploring the Crystalline Structure of Gold Mesocrystals Using X-ray Diffraction. Crystals *13*, 1204.

15. Lapkin, D., Singh, S., Kirner, F., Sturm, S., Assalauova, D., Ignatenko, A., Wiek, T., Gemming, T., Lubk, A., Müller-Caspary, K., et al. (2023). Revealing the Impact of Polystyrene Functionalization of Au Octahedral Nanocrystals of Different Sizes on the Formation and Structure of Mesocrystals. ChemNanoMat *9*, e202300336. https://doi.org/10.1002/cnma.202300336.

16. Moretti, C., Goldmann, C., Imperor-Clerc, M., and Abécassis, B. (2023). Gold Nanoparticle Superlattices: Conditions for Long-Range Order, Moiré Patterns, and Binary Phase from a Single Population. Chem. Mater. *35*, 6637–6650. https://doi.org/10.1021/acs.chemmater.3c00287.

17. Gong, J., Newman, R.S., Engel, M., Zhao, M., Bian, F., Glotzer, S.C., and Tang, Z. (2017). Shape-dependent ordering of gold nanocrystals into large-scale superlattices. Nat. Commun. *8*, 14038. https://doi.org/10.1038/ncomms14038.

18. Wochner, P., Gutt, C., Autenrieth, T., Demmer, T., Bugaev, V., Ortiz, A.D., Duri, A., Zontone, F., Grübel, G., and Dosch, H. (2009). X-ray cross correlation analysis uncovers hidden local symmetries in disordered matter. Proc. Natl. Acad. Sci. USA *106*, 11511–11514. https://doi.org/10.1073/pnas.0905337106.

19. Altarelli, M., Kurta, R.P., and Vartanyants, I.A. (2010). X-ray cross-correlation analysis and local symmetries of disordered systems: General theory. Phys. Rev. B *82*, 104207. https://doi.org/10.1103/PhysRevB.82.104207.

20. Zaluzhnyy, I.A., Kurta, R.P., Scheele, M., Schreiber, F., Ostrovskii, B.I., and Vartanyants, I.A. (2019). Angular X-ray Cross-Correlation Analysis (AXCCA): Basic Concepts and Recent Applications to Soft Matter and Nanomaterials. Materials *12*, 3464.

21. Ding, W., Xia, Y., Song, H., Li, T., Yang, D., and Dong, A. (2024). Macroscopic Superlattice Membranes Self-Assembled from Gold Nanobipyramids with Precisely Tunable Tip Arrangements for SERS. Angew. Chem. Int. Ed. Engl. *63*, e202401945. https://doi.org/10.1002/anie.202401945.

22. Miao, J., Charalambous, P., Kirz, J., and Sayre, D. (1999). Extending the methodology of X-ray crystallography to allow imaging of micrometre-sized non-crystalline specimens. Nature *400*, 342–344. https://doi.org/10.1038/22498.

23. Miao, J., Ishikawa, T., Robinson, I.K., and Murnane, M.M. (2015). Beyond crystallography: Diffractive imaging using coherent x-ray light sources. Science *348*, 530–535. https://doi.org/10.1126/science.aaa1394.

24. Vartanyants, I.A., and Yefanov, O.M. (2015). Coherent X-Ray Diffraction Imaging of Nanostructures (Pan Stanford Publishing).

25. Robinson, I., and Harder, R. (2009). Coherent X-ray diffraction imaging of strain at the nanoscale. Nat. Mater. *8*, 291–298. https://doi.org/10.1038/nmat2400.

26. Miao, J. (2025). Computational microscopy with coherent diffractive imaging and ptychography. Nature *637*, 281–295. https://doi.org/10.1038/s41586-024-08278-z.

27. Shabalin, A.G., Meijer, J.M., Dronyak, R., Yefanov, O.M., Singer, A., Kurta, R.P., Lorenz, U., Gorobtsov, O.Y., Dzhigaev, D., Kalbfleisch, S., et al. (2016). Revealing Three-Dimensional Structure of an Individual Colloidal Crystal Grain by Coherent X-Ray Diffractive Imaging. Phys. Rev. Lett. *117*, 138002. https://doi.org/10.1103/PhysRevLett.117.138002.

28. Michelson, A., Minevich, B., Emamy, H., Huang, X., Chu, Y.S., Yan, H., and Gang, O. (2022). Three-dimensional visualization of nanoparticle lattices and multimaterial frameworks. Science *376*, 203–207. https://doi.org/10.1126/science.abk0463.

29. Sun, Y., and Singer, A. (2024). Bragg coherent diffractive imaging for defects analysis: Principles, applications, and challenges. Chem. Phys. Rev. *5*, 031310. https://doi.org/10.1063/5.0219030.

30. Carnis, J., Kirner, F., Lapkin, D., Sturm, S., Kim, Y.Y., Baburin, I.A., Khubbutdinov, R., Ignatenko, A., Iashina, E., Mistonov, A., et al. (2021). Exploring the 3D structure and defects of a self-assembled gold mesocrystal by coherent X-ray diffraction imaging. Nanoscale *13*, 10425–10435. https://doi.org/10.1039/D1NR01806J.

31. Herran, M., Juergensen, S., Kessens, M., Hoeing, D., Köppen, A., Sousa-Castillo, A., Parak, W.J., Lange, H., Reich, S., Schulz, F., and Cortés, E. (2023). Plasmonic bimetallic two-dimensional supercrystals for H2 generation. Nat. Catal. *6*, 1205–1214. https://doi.org/10.1038/s41929-023-01053-9.

32. Mann, M.E., Yadav, P., and Kim, S. (2021). Colloidal Plasmonic Nanocubes as Capacitor Building Blocks for Multidimensional Optical Metamaterials: A Review. ACS Appl. Nano Mater. *4*, 9976–9984. https://doi.org/10.1021/acsanm.1c02211.

33. Schulz, F., Pavelka, O., Lehmkühler, F., Westermeier, F., Okamura, Y., Mueller, N.S., Reich, S., and Lange, H. (2020). Structural order in plasmonic superlattices. Nat. Commun. *11*, 3821. https://doi.org/10.1038/s41467-020-17632-4.

34. Wei, A., Kim, B., Sadtler, B., and Tripp, S.L. (2001). Tunable Surface-Enhanced Raman Scattering from Large Gold Nanoparticle Arrays. ChemPhysChem *2*, 743–745. https://doi.org/10.1002/1439-7641(20011217)2:12<743::AID-CPHC743>3.0.CO;2-1.

35. Fienup, J.R. (1982). Phase retrieval algorithms: a comparison. Appl. Opt. *21*, 2758–2769. https://doi.org/10.1364/AO.21.002758.

36. Lapkin, D., Shabalin, A., Meijer, J.-M., Kurta, R., Sprung, M., Petukhov, A. V., and Vartanyants, I.A. (2022). Angular X-ray cross-correlation analysis applied to the scattering data in 3D reciprocal space from a single crystal. IUCrJ *9*, 425–438. https://doi.org/10.1107/S2052252522004250.

37. Williamson, G.K., and Hall, W.H. (1953). X-ray line broadening from filed aluminium and wolfram. Acta Metall. *1*, 22–31. https://doi.org/10.1016/0001-6160(53)90006-6.

38. O'Brien, M.N., Lin, H.-X., Girard, M., Olvera de la Cruz, M., and Mirkin, C.A. (2016). Programming Colloidal Crystal Habit with Anisotropic Nanoparticle Building Blocks and DNA Bonds. J. Am. Chem. Soc. *138*, 14562–14565. https://doi.org/10.1021/jacs.6b09704.

39. Calcaterra, H.A., Zheng, C.Y., Seifert, S., Yao, Y., Jiang, Y., Mirkin, C.A., Deng, J., and Lee, B. (2023). Hints of Growth Mechanism Left in Supercrystals. ACS Nano *17*, 15999–16007. https://doi.org/10.1021/acsnano.3c04365.

40. Romanowski, W. (1969). Equilibrium forms of very small metallic crystals. Surf. Sci. *18*, 373–388. https://doi.org/10.1016/0039-6028(69)90180-0.

41. Sunagawa, I. (2005). Crystals: Growth, Morphology, and Perfection (Cambridge University Press), pp. 1–295. https://doi.org/10.1017/CBO9780511610349.

42. Chernov, A.A., Givargizov, E.J., Bagdasarov, K.S., Kuznetsov, V.A., Demianets, L.N., and Lobachev, A.N. (2012). Modern Crystallography III: Crystal Growth (Springer Berlin Heidelberg).

43. Kaye, A., Stepto, R.F.T., Work, W.J., Alemán, J.V., and Malkin, A.Y. (1998). Definition of terms relating to the non-ultimate mechanical properties of polymers (Recommendations 1998). Pure Appl. Chem. *70*, 701–754. https://doi.org/10.1351/pac199870030701.

44. Zhou, S., Li, J., Lu, J., Liu, H., Kim, J.-Y., Kim, A., Yao, L., Liu, C., Qian, C., Hood, Z.D., et al. (2022). Chiral assemblies of pinwheel superlattices on substrates. Nature *612*, 259–265. https://doi.org/10.1038/s41586-022-05384-8.

45. Park, B.C., Ko, M.J., Kim, Y.K., Kim, G.W., Kim, M.S., Koo, T.M., Fu, H.E., and Kim, Y.K. (2022). Surface-ligand-induced crystallographic disorder–order transition in oriented attachment for the tuneable assembly of mesocrystals. Nat. Commun. *13*, 1144. https://doi.org/10.1038/s41467-022-28830-7.

46. Weckert, E. (2015). The potential of future light sources to explore the structure and function of matter. IUCrJ *2*, 230–245. https://doi.org/10.1107/S2052252514024269.

47. Schroer, C.G., Wille, H.-C., Seeck, O.H., Bagschik, K., Schulte-Schrepping, H., Tischer, M., Graafsma, H., Laasch, W., Baev, K., Klumpp, S., et al. (2022). The synchrotron radiation source PETRA III and its future ultra-low-emittance upgrade PETRA IV. Eur. Phys. J. Plus *137*, 1312. https://doi.org/10.1140/epjp/s13360-022-03517-6.

48. Kirner, F., Potapov, P., Schultz, J., Geppert, J., Müller, M., González-Rubio, G., Sturm, S., Lubk, A., and Sturm, E. (2020). Additive-controlled synthesis of monodisperse single crystalline gold nanoparticles: interplay of shape and surface plasmon resonance. J. Mater. Chem. C Mater. *8*, 10844–10851. https://doi.org/10.1039/D0TC01748E.

49. Favre-Nicolin, V., Girard, G., Leake, S., Carnis, J., Chushkin, Y., Kieffer, J., Paleo, P., and Richard, M.-I. (2020). PyNX: high-performance computing toolkit for coherent X-ray imaging based on operators. J. Appl. Crystallogr. *53*, 1404–1413. https://doi.org/10.1107/S1600576720010985.

50. Fienup, J.R. (1978). Reconstruction of an object from the modulus of its Fourier transform. Opt. Lett. *3*, 27–29. https://doi.org/10.1364/OL.3.000027.

51. Marchesini, S. (2007). Invited Article: A unified evaluation of iterative projection algorithms for phase retrieval. Rev. Sci. Instrum. *78*, 011301. https://doi.org/10.1063/1.2403783.

52. Gerchberg, R.W., and Saxton, W.O. (1972). A practical algorithm for the determination of phase from image and diffraction plane pictures. Optik *35*, 237–246.

53. Clark, J.N., Huang, X., Harder, R., and Robinson, I.K. (2012). High-resolution three-dimensional partially coherent diffraction imaging. Nat. Commun. *3*, 993. https://doi.org/10.1038/ncomms1994.

54. Marchesini, S., He, H., Chapman, H.N., Hau-Riege, S.P., Noy, A., Howells, M.R., Weierstall, U., and Spence, J.C.H. (2003). X-ray image reconstruction from a diffraction pattern alone. Phys. Rev. B *68*, 140101. https://doi.org/10.1103/PhysRevB.68.140101.

55. Favre-Nicolin, V., Leake, S., and Chushkin, Y. (2020). Free log-likelihood as an unbiased metric for coherent diffraction imaging. Sci. Rep. *10*, 2664. https://doi.org/10.1038/s41598-020-57561-2.

56. Chapman, H.N., Barty, A., Marchesini, S., Noy, A., Hau-Riege, S.P., Cui, C., Howells, M.R., Rosen, R., He, H., Spence, J.C.H., et al. (2006). High-resolution ab initio three-dimensional x-ray diffraction microscopy. J. Opt. Soc. Am. A *23*, 1179–1200. https://doi.org/10.1364/JOSAA.23.001179.